

Available online at [www.sciencedirect.com](http://www.sciencedirect.com)

ScienceDirect

journal homepage: [www.elsevier.com/locate/AJPS](http://www.elsevier.com/locate/AJPS)

Original Research Paper

# Bone mesenchymal stem cell-derived exosomes involved co-delivery and synergism effect with icariin via mussel-inspired multifunctional hydrogel for cartilage protection



Jia Zeng<sup>a</sup>, Peng Sun<sup>a</sup>, Yuanqian Zhao<sup>a</sup>, Xinning Fang<sup>a</sup>, Zhenghong Wu<sup>a,\*</sup>, Xiaole Qi<sup>a,b,\*</sup>

<sup>a</sup>Key Laboratory of Modern Chinese Medicines, China Pharmaceutical University, Nanjing 210009, China

<sup>b</sup>Industrial Technology Innovation Platform, Zhejiang Center for Safety Study of Drug Substances, Hangzhou 310018, China

## ARTICLE INFO

### Article history:

Received 27 December 2022

Revised 2 February 2023

Accepted 8 March 2023

Available online 31 March 2023

### Keywords:

Osteoarthritis

Icariin

Exosomes

Multifunctional hydrogel

## ABSTRACT

Mesenchymal stem cells (MSC) are particularly effective in promoting cartilage regeneration due to their immunomodulatory, anti-inflammatory and regenerative repair functions of tissues and organs. Meanwhile, the intra-articular delivery and synergy with other therapeutic drugs have been the key issues driving their further application. We report a mussel-inspired multifunctional hydrogel system, which could achieve co-delivery and synergism effect of MSC-derived exosomes (Exos) with icariin (ICA). The ICA and Exos co-delivered articular cavity injection system are expected to retain in the joint cavity and promote cartilage regeneration, due to the thermosensitive, self-healing and adhesion properties of the mussel-inspired multifunctional hydrogel. The experimental results proved that Exos enhanced the cellular uptake of ICA by more than 2-fold evenly, and the synergism of Exos and ICA efficiently improve the cell proliferation and migration. After synergic treatment, the content of matrix metalloproteinase 13 in the supernatant and intracellular decreased by 47% and 59%, respectively. *In vivo* study, ICA-loaded Exos exhibited prolonged retention behavior by multifunctional hydrogel delivery, thus displayed an increased cartilage protection. In the model of osteoarthritis, co-delivery hydrogel system relieved the cartilage recession, ensuring appropriate cartilage thickness.

© 2023 Shenyang Pharmaceutical University. Published by Elsevier B.V.

This is an open access article under the CC BY-NC-ND license

(<http://creativecommons.org/licenses/by-nc-nd/4.0/>)

## 1. Introduction

Osteoarthritis (OA) is the most common chronic disabling disease, and its incidence is increasing rapidly. OA is a

comprehensive joint disease with complex pathogenesis, including multiple structural changes, of which cartilage degeneration is typical [1,2]. And the metabolic disorders of chondrocytes and extracellular matrix (ECM) are the main characteristic of the destruction of articular cartilage

\* Corresponding authors.

E-mail addresses: [zhenghongwu66@cpu.edu.cn](mailto:zhenghongwu66@cpu.edu.cn) (Z.H. Wu), [qixiaole523@cpu.edu.cn](mailto:qixiaole523@cpu.edu.cn) (X.L. Qi).

Peer review under responsibility of Shenyang Pharmaceutical University.

<https://doi.org/10.1016/j.ajps.2023.100799>

1818-0876/© 2023 Shenyang Pharmaceutical University. Published by Elsevier B.V. This is an open access article under the CC BY-NC-ND license (<http://creativecommons.org/licenses/by-nc-nd/4.0/>)

[3–5]. In the OA chondrocytes, the expression of matrix metalloproteinases (MMP) is significantly up-regulated, which could induce ECM degradation and chondrocyte composition changes [6–8]. There is no distribution of blood vessels, nerves or lymphatic vessels in cartilage tissue, hence the self-repair ability is extremely limited. However, existing clinical treatment strategies only relieve symptoms, but fail to target pathogenesis and reverse cartilage damage [9,10].

Icariin (ICA) is the main biologically active pharmaceutical ingredient of Chinese herb *Epimedium* [11]. Numerous studies have demonstrated a wide range of pharmacological effects of ICA in multiple indications, including bone regeneration promotion [12–14], neuroprotection [15,16] and antitumor effects [17]. Additionally, ICA could significantly induce chondrogenic differentiation of stem cell, promote chondrocytes proliferation and related genes expression, reduce the expression of MMP, and enhance the secretion of ECM, thus enhancing cartilage repair [18–20]. It's found that the regulation of ICA is multi-targeting through mediating of NF- $\kappa$ B, Wnt/ $\beta$ -catenin, MAPK and other signaling pathways [21,22]. However, the low solubility and permeability of ICA limit its clinical application [18].

Recently, mesenchymal stem cell (MSC)-based therapy has raised considerable concern in cartilage regeneration, of which the trophic and immunomodulatory properties influence the cell activity, but the severe immune rejection makes it a huge risk [23,24]. In addition to their cell forms, the MSC secretome can also be exploited in the form of exosomes (Exos), and cell membrane can be directly used as drug carrier [24]. Moreover, MSCs have been verified that their immune modification is achieved by the Exos signaling pathway [25]. Exos are cell-derived membrane vesicle and contain abundant active component, providing stable mediums for cell-cell communication [26–28]. Some studies have revealed the chondrogenic repair and anti-inflammatory effects of bone marrow mesenchymal stem cells (BMSCs)-derived Exos, confirming the possibility of “cell-free” therapy strategy for OA [29–31]. Furthermore, Exos are the primary mediators of paracrine, which is commonly involved in cartilage repair in MSCs with adjacent cells [32], hence, Exos are capable of functionally transferring biological information. The potential vehicles functions of Exos have been widely applied in drug delivery, including proteins, RNA, small-molecular drugs and so on. As natural delivery carriers, Exos have multiple advantages. The membrane composition of Exos is highly similar to cell membranes, giving them high biosafety and the ability to overcome natural barriers [33–35]. Nevertheless, the poor accumulation of Exos in the arthrosis lesion site decreased the efficiency due to the rapid clearance [36–38]. The regeneration of defective cartilage commonly goes through a complicated and lengthy period [39], herein it is essential to enhance the retention and sustained release of Exos in target region [40].

Biocompatible hydrogels possess unique properties highly similar to cartilage ECM, providing 3D microenvironments for cell growth, differentiation and migration [29,41–43]. Hydrogels with suitable mechanical strength serve as temporary implants, which would be eventually replaced by new cartilage tissue [44,45]. The structural composition and abundant properties of hydrogels were sufficiently

adjustable to fit different organizational characteristics. Hydrogels combining with cells, growth factors and other active molecules have shown superior potential to cope with the challenges of cartilage defects in OA. The high therapeutic efficiency is attributed to the protection and retention of active ingredient by hydrogels, of which the porous structures along with mild biodegradability further ensure the controlled release of active ingredients [46–48].

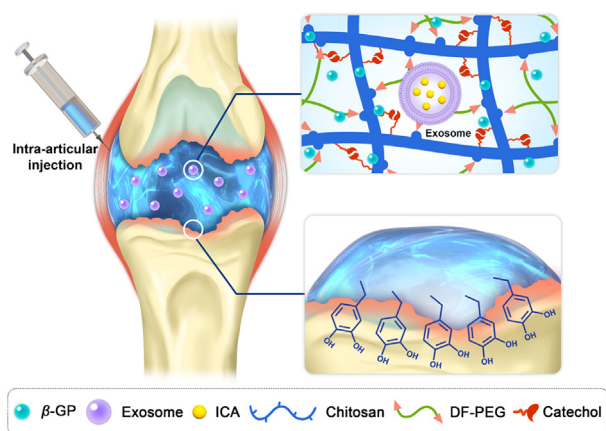
Although some Exos-laden hydrogels have been used in cartilage regeneration, the lack of multifunctional modification of hydrogels and the single therapeutic effect of Exos great limits their further application [49–51]. In our previous study, we have designed a thermosensitive and self-healing hydrogel [52]. Thermosensitivity enables hydrogels to respond quickly to temperature changes, allowing gels to be injected intra-articular in the minimally invasive manner with rapid actions and less side effects [53,54]. Simultaneously, self-healing ability ensures the structural integrity of gels even in active regions of frequent movements [55]. Nevertheless, this gel still failed to solve the problem that traditional hydrogels have trouble sticking to wet tissue surfaces. Encouragingly, in recent years, “mussel-inspired” materials have aroused great interests because of their unique adhesive property, owing to a large number of catechol groups, which can interact with a variety of groups and form tight adhesion [56–58]. Therefore, hydrogel containing catechol groups might execute better wet adhesion.

Herein, in order to exert the excellent cartilage repair effect of ICA, Exos-based delivery vehicle was designed. The stability and cell affinity of BMSCs-Exos carrier were used to improve the ICA uptake efficiency of target cells. At the same time, we coordinately delivered ICA and Exos, creating synergies of the two in cartilage repair, including the protection of chondrocytes and the inhibition of MMP secretion. And to further improve the retention behavior of ICA@Exos, the thermosensitive, self-healing and adhesive hydrogel was prepared and selected as intra-articular delivery medium. The multifunctional hydrogel was based on chitosan (CS) skeleton, and the temperature-sensitive system was constructed by mixing with  $\beta$ -glycerophosphate disodium salt hydrate ( $\beta$ -GP). Dialdehyde-functionalized polyethylene glycol (DF-PEG) was used as dynamic crosslinkers, endowing gels with excellent self-healing ability. In addition, the introduction of catechol groups improved the tissue adhesion of hydrogel system, and the non-covalent bonds between catechol groups enhanced the self-healing ability. The completely ICA@Exos-loaded hydrogel system is exhibited in [Scheme 1](#). In general, this system fully exploited the therapeutic advantages of each component. Finally, the efficient cartilage protection of ICA@Exos-loaded “mussel inspired” multifunctional gels was verified by *in vivo* and *in vitro* experiments in detail.

## 2. Materials and methods

### 2.1. Materials

Exosome depleted Fetal Bovine Serum (FBS) was purchased from Vivacell (Germany). Antibodies such as APC Anti-Mouse CD45, HSP70 Antibody and MMP13 antibody were all obtained



**Scheme 1 – Schematic of ICA@Exos-loaded hydrogel system for the cartilage repair and regeneration in OA treatment.**

from Proteintech (Wuhan, China). Chlorpromazine (CPZ), genistein (GST) and amiloride (AMI) were gained from Macklin (Shanghai, China). Icarin and Coumarin 6 (C6) were separately bought from Shanghai Yuanye Co., Ltd. (Shanghai, China) and Sigma-Aldrich (USA). IL-1 $\beta$  was purchased from PeproTech (USA). Chitosan was offered by Zhejiang Aoxing Biotechnology Co., Ltd. (Taizhou, China). All chemicals were used as received without further purification.

## 2.2. Derivation and identification of BMSCs

Primary BMSCs were extracted from 3-week-old C57BL/6 mice's femurs and tibias. BMSCs were cultured in DMEM medium supplemented with 10% FBS at 37 °C, 5% CO<sub>2</sub> incubator. Then P3 cells were used for phenotype identification. Firstly, to detect cell surface marker proteins, BMSCs were combined with polyclonal antibodies CD11b, CD45, CD90 and CD105, analyzed by flow cytometry (FCM). Next, for determining the osteogenic differentiation ability of BMSCs, cells were cultured in osteogenic induction medium for 21 d, followed by Alizarin Red staining.

## 2.3. Isolation and characterization of BMSCs-Exos

Exosome-free FBS was added in cell culture medium, and when BMSCs grown to a suitable cell density, the culture supernatant was collected. Then, Exosome Isolation Kit (Umibio, China) was selected to isolate Exos efficiently, of which the operation was in accordance with the instructions. The morphologies and structures of obtained Exos was observed under transmission electron microscopy (TEM), while the particle size distribution was detected by nanoparticle tracking analysis (NTA). Additionally, antibodies against CD81 and HSP70 were utilized to identify the expression of characteristic proteins by western blot (WB).

## 2.4. Drug-loaded properties of BMSCs-Exos

To prepare ICA@Exos, Freeze-Thaw Cycle Method was selected. ICA was mixed and incubated with Exos in different

mass ratios at RT, rapidly frozen in liquid nitrogen for 90 s, and then re-thawed at RT. This freeze-thaw cycle was repeated 3 times. At the end of the cycle, mixed solution was centrifuged at 4 °C at 16,000 g for 20 min to separate the unloaded ICA, obtaining ICA@Exos. After this, an appropriate amount of ICA@Exos was mixed with methanol to destroy the Exos' structures and release ICA, of which the concentration was determined by high performance liquid chromatography (HPLC). Simultaneously, the morphological structure and particle size distribution of exosomes after drug-loaded were further studied.

## 2.5. In vitro drug release behavior of ICA@Exos

Here, the in vitro drug release behavior of ICA@Exos in PBS (pH 7.4) release medium was investigated. Appropriate amount of ICA@Exos solution was transferred into a dialysis bag (MWCO:3.5 KDa) and placed in PBS. The whole apparatus was shaken at 100 rpm in a 37 °C constant temperature shaker. The release medium was collected at predetermined time points (0.5, 1, 1.5, 2, 4, 8, 18, 24 h) and the supernatant was taken for ICA concentration determination to investigate in vitro drug release behavior of ICA@BMSCs-Exos.

## 2.6. Cellular uptake efficiency and endocytosis mechanism

In related cell experiments, SW1353 cells were selected as OA cell models. SW1353 cells have been confirmed to possess a typical chondrocyte phenotype, and have been widely applied to the study of chondrocyte function, especially OA researches [59,60]. SW1353 cells were cultured in a 37 °C incubator under 90% humidity without CO<sub>2</sub>. The cellular uptake efficiency and endocytosis mechanism were qualitatively and quantitatively evaluated by confocal laser scanning microscope (CLSM) and FCM. Additionally, a liposoluble fluorescence probe (C6), was used instead of ICA to investigate the cellular uptake behavior. Experiments were divided into two groups: free C6 group and C6@Exos group, then each group was further separated into four time points: 0.5, 1, 2 and 4 h. The concentration of C6 in each group was 20 ng/ml, determined by fluorescence spectrophotometer.

Firstly, cells were seeded, then were treated with C6 separately at a preset time. After incubation and PBS washing, cells were fixed with 4% paraformaldehyde and stained by nuclear dye (Hoechst 33342, 10  $\mu$ g/ml). The treated cells were washed again and kept in PBS. Detected by CLSM, the images showed the distribution of C6 in cells. Secondly, for FCM analysis, cells were seeded. After C6 treatment, cells were washed and digested, then resuspended in PBS for sample loading. All the above operations should be carefully shielded from light.

To further confirm the endocytosis mechanism of Exos, three kinds of endocytosis inhibitors, including CPZ, GST and AMI, were utilized to intervenes cells. Beforehand, the cytotoxicity of each inhibitor was examined by MTT assay, to ensure their biosafety without effect on cellular uptake. Then SW1353 cells were cultured with different inhibitors for 1 h in advance. Subsequently, inhibitors were replaced by C6@Exos,

and cells were cultured for another 4 h. Cells were washed and collected, detecting by FCM.

## 2.7. Proliferation and migration effects

Interleukin-1 $\beta$  (IL-1 $\beta$ ) could induce the formation of OA cell models. Therefore, in the following experiments, IL-1 $\beta$  (10 ng/ml) were added into cell culture medium, to mimic the inflammatory environment for SW1353 cells. Firstly, cells were cultured with free ICA to estimate the optimal proliferation promoting concentration of ICA. In the experiments, cells were divided into blank group, control group and experimental group with different ICA concentration ( $10^{-8}$ ,  $10^{-7}$ ,  $10^{-6}$ ,  $10^{-5}$  and  $10^{-4}$   $\mu$ M). After incubation for 24 h, the proliferation rate of cells in each group was detected by MTT cell proliferation kit (KeyGene, China). Then, the appropriate ICA concentration was determined to further investigate the promoting effects of ICA, Exos and ICA@Exos on cell proliferation.

Moreover, for migration evaluation, cells were seeded on 6-well plates, and a scratch was made by 200  $\mu$ l pipette tips. Subsequently, mediums containing ICA, Exos and ICA@Exos, respectively, were then added to the scratched wells. At 0, 6, 12 and 24 h, the cell migration was photographed and the images were analyzed by Image J.

## 2.8. Inhibition of MMP13 secretion

To evaluate the MMP13 expression level, cells were cultured with ICA, Exos and ICA@Exos separately, under the inflammatory condition caused by IL-1 $\beta$ . After incubation for 24 h, cell supernatants and intracellular proteins were collected. MMP13 in the supernatants was measured quantitatively by ELISA Kit (MultiSciences, China) according to the manufacturer's instructions. While, intracellular MMP13 was tested semiquantitative through WB.

## 2.9. Synthesis and verification of CAT-C and DF-PEG

To synthesize catechol-modified chitosan (CAT-C), the chemical reactions are supplied in Fig. S1. 0.5 g CS was fully dissolved in 50 ml HAc solution (0.1 M), stirring and dropping 1 M NaOH solution, to form a "cloudy" turbidity. Then 0.59 g hydrocaffeate (HCA) was added. 1.224 g EDC was weighed and completely dissolved in 46 ml 50% ethanol solution, then continuously adding to the above CS solution. In the adding process, pH of the system was maintained at  $\sim$ 4.6. After 90 min of stirring reaction, the system was transferred into a dialysis bag (MWCO:14 KDa), dialyzing in 100 mM NaCl solution (pH 3.3) for 2 d. Lastly, deionized water (pH 5.0) was replaced as dialysis medium for 4 h. The final product was obtained by lyophilization. As for the preparation of DF-PEG, the method referred to our previous study [52], of which the chemical reactions are supplied in Fig. S2. In the process of product identification, fourier transform infrared spectroscopy (FTIR), ultraviolet spectroscopy (UV) and nuclear magnetic resonance (NMR) were utilized. Supplementarily, for NMR analysis, CAT-C and DF-PEG were respectively dissolved in deuterated water and deuterated chloroform.

## 2.10. Preparation and morphology analysis of hydrogel

Concisely, 2.5% CS solution (dissolved in 0.1 M HAc), 2.5% CAT-C solution (dissolved in 0.1 M HAc), 60%  $\beta$ -GP solution and 15% DF-PEG solution were prepared separately. Under continuous ice bath stirring,  $\beta$ -GP aqueous solution was dropped into the uniform mixture of CS and CAT-C. Lastly, DF-PEG aqueous solution was added, and the obtained hydrogel precursor solution was stored at 4  $^{\circ}$ C. In this hydrogel system, the final concentrations of each component were as follows: 1.30% CS, 0.43% CAT-C, 18.13%  $\beta$ -GP and 0.106% DF-PEG.

The morphologies of hydrogels were observed by a scanning electron microscope (SEM). The precursor gel solutions were incubated at 37  $^{\circ}$ C for 1 h, then the obtained gels were lyophilized. The lyophilizate was cut in a suitable manner and coated by ion sputter gold. The morphologies were observed and the pictures were taken.

## 2.11. Multifunctional characterizations of hydrogel

To verify the thermos-sensitivity of gels, gel precursor solutions were added into a penicillin bottle, followed with heating at 37  $^{\circ}$ C. The state changes before and after heating were investigated by macroscopic observation. Additionally, the gelation transition temperature ( $T_{\text{sol-gel}}$ ) was further evaluated by rheological measurement. The phase lag ( $\delta$ ) was taken to determine the  $T_{\text{sol-gel}}$  at which elastic modulus ( $G'$ ) and viscous modulus ( $G''$ ) were equivalent in value ( $\delta = 45^{\circ}$ ). Similarly, the self-healing property was also estimated from macroscopic and rheological perspectives. The red stained gels were placed close to the blank gels, to investigate if the two would spontaneously cross-link. Subsequently, the changes of gel modulus were evaluated through repeated dynamic strain step tests (strain is switched from 0.05% to 50% to 0.05%, for two cycles). Furthermore, the mussel-inspired adhesion of gels on glass surfaces was also measured. Two slides were glued together with gels, to test the ability to support a certain weight.

## 2.12. In vitro degradation and in vivo gelation investigation of hydrogel

The *in vitro* degradation behavior of blank gels was determined by simulating the liquid environment of joint cavity with lysozyme solution. The research objects included CCGD gels (referred to blank gels) and CCG gels (referred to gels without DF-PEG). 1 ml sample gels were prepared, fully gelled in a pre-weighed centrifuge tube ( $M_{\text{tube}}$ ), then weighed ( $M_0$ ). The two experimental groups were divided into 8 time point, and each time point was set with 3 parallel controls. The lysozyme solution (0.2 mg/ml in pH 7.4 PBS) was added to each tube and shaken at  $100 \pm 5$  rpm at 37  $^{\circ}$ C. At scheduled time, tubes were taken out and the supernatant were removed. The remaining gels and tubed were weighed ( $M_t$ ). The residual degradation rat of gels was calculated by the following formula:

$$\text{Residual degradation (\%)} = (M_t - M_{\text{tube}})/(M_0 - M_{\text{tube}}) \times 100\%$$

Additionally, *in vivo* gelation investigation was carried out in CCGD gels, CCG gels and CGD gels (refereed to gels without

CAT-C). Experiments were performed by subcutaneous administration into the back of a Sprague-Dawley rat. 300  $\mu$ l CCGD (red stained), CCG (blue stained), CGD (yellow stained) gel precursor solutions were subcutaneously injected, respectively. 5 min later, the rats were sacrificed, and the injection site was cut. The gels state was then observed, both wrapped in and peeled from the skin. Meanwhile, the adhesion of peeled hydrogel was further tested.

### 2.13. *In vitro safety evaluation of hydrogel*

The cytotoxicity and hemolysis of hydrogel extractive solutions were evaluated, firstly. SW1353 cells was used as research objects, and Leibovitz's L-15 medium was selected to prepare extractive solutions. Different volumes of gels were immersed for 48 h, then the immersed medium was filtered to obtain hydrogel extractive solutions with concentrations of 0.05, 0.1, 0.15, 0.20, 0.25 and 0.30 g/ml. Briefly, SW1353 cells were seeded into 96-well plates and incubated for 24 h. Then medium was substituted by hydrogel extractive solutions, and cultured for another 24 h. According to the instructions of MTT kit, the cell viability was measured. For hemolysis assay, 2% blood cell suspension was pre-prepared by centrifuging and washing fresh rat whole blood. 0.1, 0.2 and 0.4 mg/ml hydrogel extractive solutions were separately mixed with the same volume of blood cell suspension, and incubated at 37 °C for 4 h. Subsequently, the supernatant was detected by UV at 540 nm, while deionized water and 0.9% saline were set as control.

Furthermore, the cell growth condition, when 3D cultured inside hydrogels, was observed. Hydrogel precursor solutions was added into 24-well plates, heating at 37 °C until complete gelled, and then were exposed to ultraviolet for sterilization. 500  $\mu$ l medium was added to each well for hydrogel infiltration. After 1 h, blank medium was replaced by SW1353 cell suspension, and cultured within the schedule time. After a gentle wash, 250  $\mu$ l Calcein AM staining solution were evenly tiled on hydrogels, and incubated at 37 °C for 45 min. Afterwards, hydrogels were incubated again with pre-heated medium for another 30 min, to ensure that Calcein AM could be fully hydrolyzed to form green fluorescent Calcein for living cell staining. The cellular distribution inside hydrogels was observed by cell imaging system.

### 2.14. *Drug-loaded properties of hydrogel*

The ICA@Exos-loaded hydrogel was prepared by referring to the above method, and the final concentration of ICA was 30  $\mu$ g/ml. In order to exhibit the distribution of ICA@Exos inside hydrogels, Exos was fluorescently labeled with Dio in advance. In brief, Exos solution was mixed with Dio solution, of which the concentration was 5  $\mu$ M. Incubating for 20 min, the unbound dye was removed through membrane filtration. Subsequently, the 3D distribution of ICA@Exos inside hydrogels was investigated by CLSM.

Additionally, the drug release behavior was also evaluated, and ICA@Exos-loaded hydrogels and ICA-loaded hydrogels were prepared. 1 ml hydrogel precursor solutions were added respectively and heated until completely gelled. PBS (pH 7.4) solutions were added as release medium, and continuously

oscillated at 100 rpm and 37 °C. At specific time points (0.17, 1, 2, 3, 4, 6, 9, 13, 17, 21 and 28 d), 0.5 ml release medium were sampling analyzed and replaced with 0.5 ml fresh medium. The drug release amount of each point was measured by HPLC, and cumulative release behavior was finally obtained.

### 2.15. *In vivo safety assessment*

Briefly, the *in vivo* safety of ICA@Exos-loaded hydrogels was verified by routine blood test and Hematoxylin-Eosin (H&E) staining of skin tissue. Herein, experiment objects were divided into three groups: saline group, blank hydrogels group and ICA@Exos-loaded hydrogels group. First, 100  $\mu$ l of the above solutions were injected subcutaneously into the armpit of ICR mice, respectively. The body weight of mice in three groups was monitored within 7 d consecutively, and blood samples were collected on Day 7 for routine blood test.

Next, each group was further divided into three time points on Day 1, 3 and 7. The above preparations were injected subcutaneously into the back of SD rats. The rats were sacrificed at the set time, and the dorsal skin at the injection site was taken for H&E staining. The inflammatory effect of the hydrogels was observed by section to evaluate the biological safety *in vivo*.

### 2.16. *Animal models construction*

To construct OA rat models, the SD rats were first anesthetized and then depilated at the knee joint. After disinfection, the knee was bent to expose joint plane, and the white lateral patellar tendon was selected as puncture point. A 1-ml syringe was slowly inserted vertically into the intercondylar fossa. When insertion resistance increased significantly, needle was slightly retreated, and 100  $\mu$ l of 4% papain solution was injected into the knee joint cavity. The same procedures were performed on Day 4 and 7. During the modeling, 200  $\mu$ l gentamicin solution ( $5 \times 10^4$  units/ml) was injected into the leg muscle on Day 1, 2, 3, respectively.

### 2.17. *In vivo retention of Exos by hydrogel*

In order to investigate the effect of the hydrogels on the *in vivo* retention behavior of ICA@Exos, Exos was fluorescently labeled with DiR beforehand. The DiR concentration was 1  $\mu$ M, and the labeling method was the same as above. Subsequently, 100  $\mu$ l DiR-labeled ICA@Exos and ICA@Exos-loaded hydrogel were separately injected into the knee joint of rats in different groups. On Day 1, 4 and 7, the retention behavior of Exos in the knee joint with or without hydrogels were observed by small animal *in vivo* imaging systems.

### 2.18. *In vivo pharmacodynamics*

The experiment was divided into saline group, ICA@Exos group, ICA-loaded hydrogel group and ICA@Exos-loaded hydrogel group, to investigate the pharmacodynamic effect of each preparation in the treatment of OA. Twenty OA model rats were randomly divided into four groups. 150  $\mu$ l of the above four preparations were injected *in situ* into the knee joint cavity, respectively, and then the rats were fed normally

for 5 weeks. Eventually, the rats were sacrificed and the intact knee tissues were removed and sequentially immersed in formalin solution for 48 h and EDTA-decalcification solution until complete decalcification. The tissue samples were analyzed by H&E, Safranin O-Fast Green (SO-FG), Tuloidine Blue (TB) and MMP13 immunohistochemical (IHC) staining.

### 2.19. Statistical analysis

All results were presented as mean  $\pm$  SD statistical analysis from at least three independent experiments. A two-tailed t-test was performed, and \*\*\* $P < 0.001$ , \*\* $P < 0.01$  and \* $P < 0.05$  were considered statistically significant.

## 3. Results and discussion

### 3.1. Preparation and characterization of ICA@Exos

First, the phenotype of extracted BMSCs was identified by FCM. The surface markers of BMSCs are non-specific, expressing multiple surface marker proteins, such as adhesion molecules CD44, cytokine receptors IL-1R and integrin protein CD29. Additionally, BMSCs do not express the surface markers associated with hematopoietic cells and leukocytes. The positive expression rates of CD90 and CD105 were 94.87% and 90.14%, respectively, while the negative expression rates of CD11b and CD45 were 3.65% and 1.02%, respectively. The FCM results are shown in Fig. 1A, indicating that the cell phenotype was correct and not significantly interfered by parenchymal cells. Furthermore, after osteogenic- induce, alizarin red staining results (Fig. 1B) revealed the excellent mineralization capacity of BMSCs. As ECM secretion and mineral salts deposition increased, prominent calcified nodules were formed and stained red. Two identification experiments proved that BMSCs successfully extracted possessed good purity and multidirectional differentiation ability.

After isolation from cell culture supernatant, BMSC-Exos were characterized in terms of morphology, size and marker protein expression. TEM observation exhibited that Exos owned obvious spherical morphology with a significant lipid bilayer structure (Fig. 1C). WB analysis revealed that Exos were positive for expressing exonal marker proteins, including HSP70 and CD81 (Fig. 1D). NTA results showed that the particle size distribution of EXO was normally, ranging from 30 to 150 nm, with an average particle size of about 127.4 nm (Fig. 1E). All these results indicated the collected Exos had typical morphological and molecular features.

Next, ICA@Exos were prepared by freeze-thaw cycle method, and the maximum drug loading rate was 24.08%  $\pm$  3.02% detected by HPLC. Moreover, ICA@Exos were characterized by TEM (Fig. 1F) and NTA (Fig. 1G). TEM observation showed that ICA@Exos remained spherical and still had a typical lipid bilayer structure, indicating that drug encapsulation would not destroy the structural specificity and integrity of Exos. And the approximate particle size of ICA@Exos was further verified, with an average value of about 130.0 nm. The NTA results again confirmed that drug encapsulation had little effect on the structure of Exos,

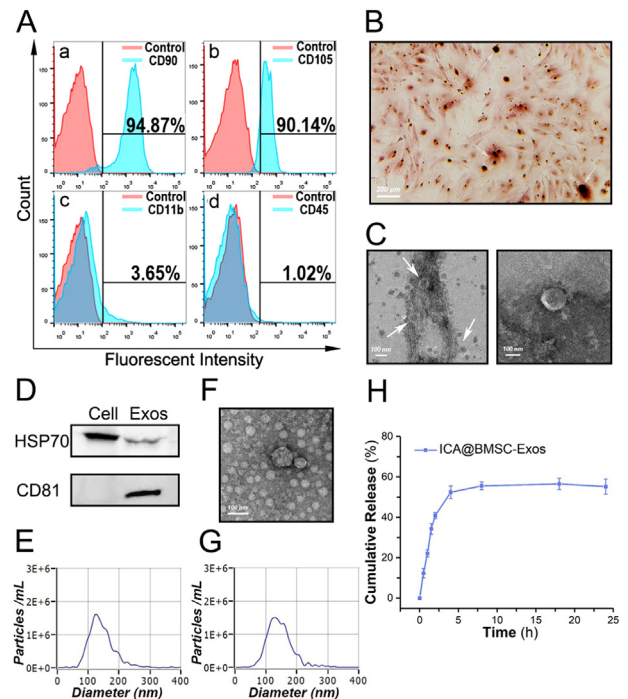


**Fig. 1 – The identification of BMSCs, characterization of BMSC-Exos, and the verification and drug release kinetics of ICA@Exos. (A) The FCM results for BMSCs identification. (B) Alizarin red staining micrographs for verifying the osteogenic differentiation ability of BMSCs. (C) TEM images of BMSC-Exos. (D) Characteristic proteins analysis of BMSC-Exos by WB. (E) NTA results of BMSC-Exos. (F-H) TEM images, NTA results and the drug release behavior of ICA@Exos.**

thus the continuity of structure ensured the reliability of its activity. In addition, the drug release curve was shown in Fig. 1H. ICA@Exos had a quick release rate in the first 8 h, with a total release quantity of nearly 55%. The release behavior of ICA@Exos demonstrated that ICA@Exos is basically stable, but the fast drug release rate limited the retention in knee joint. Therefore, it is indispensable to further construct long-acting carriers and protective barriers for ICA@Exos, forming an effective drug reservoir for OA treatment.

### 3.2. Cellular uptake efficiency and endocytosis mechanism

To illustrate the intracellular uptake efficiency of Exos, qualitative analysis using CLSM was performed, and the images were displayed in Fig. 2A. There were significant differences in uptake efficiency between free C6 and C6@Exos groups, that Exos as delivery vectors remarkably improved intracellular uptake of C6. To find out, FCM was used to further quantitatively investigated C6@Exos cellular uptake. The results of FCM are shown in Fig. 2B, and the statistical results of mean fluorescence intensity (MFI) are shown in Fig. 2C. At 0.5, 1, 2 and 4 h, the fluorescence intensity of C6 in the two groups was compared and analyzed. Consistent with the CLSM images, the intracellular uptake efficiency of C6@Exos was significantly higher than that of free C6 group,

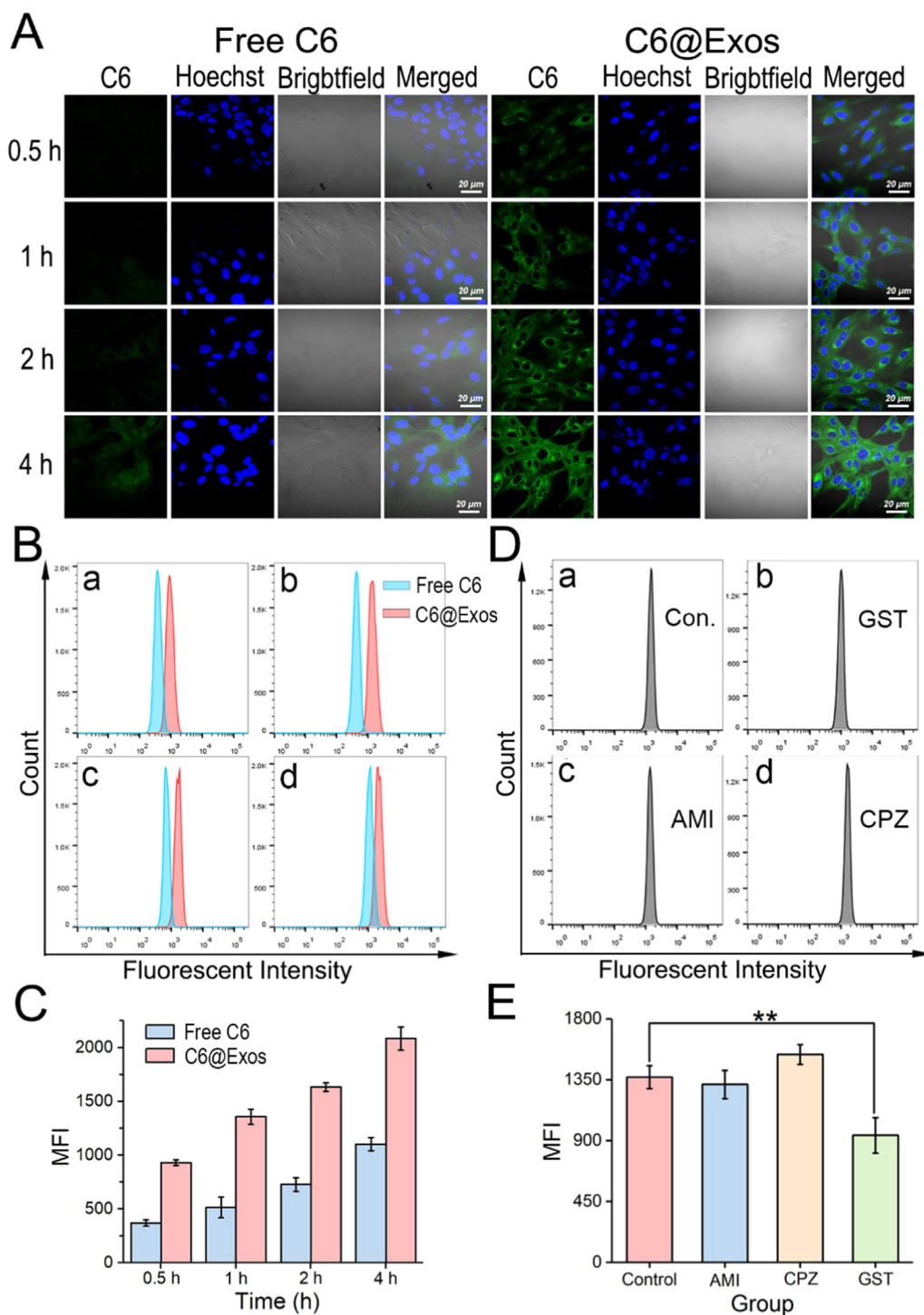


**Fig. 2 – Cellular uptake efficiency and endocytosis mechanism of ICA@Exos. (A) CLSM images of SW1533 cells after respectively incubation with free C6 and C6@Exos for 0.5, 1, 2 and 4 h (green refers to C6, and blue refers to nucleus). (B-C) FCM results and statistical graphs of cellular uptake investigation of free C6 and C6@Exos (a, b, c and d refer to 0.5, 1, 2 and 4 h). (D-E) FCM results and statistical graphs of endocytosis mechanism study. Statistical significance: \*\* $P < 0.01$ .**

which was increased by 2.51, 2.63, 2.24 and 1.89 times at each time points, respectively. The high uptake efficiency was attributed to the efficient cellular delivery effects of Exos. The lipid bilayer membrane makes Exos possess higher affinities with cells, thereby facilitating hypotonic drugs

entry. Then, by analyzing the cellular uptake efficiency at different time points within the same group, it was found that drugs were gradually accumulated in cells at a decreasing uptake rate. Hypothetically, the entry of Exos into cells is an active transport process, requiring the participation

of multiple channel proteins on the cell membrane. As cellular uptake continues, the channel proteins became saturated, so that the uptake rate decreased with the time of uptake.

Herein, to understand the internalization mechanism, we added different endocytosis inhibitors, including CPZ (clathrin-mediated endocytosis-inhibiting), GST (caveolin-mediated endocytosis-inhibiting) and AMI (macropinocytosis-mediated endocytosis-inhibiting), then further measured the relative uptake efficiency of Exos. Firstly, the cytotoxicity of each inhibitor was evaluated in order to avoid its possible toxicity that could interfere with cellular uptake. As shown in Fig. S3, the MTT results exhibited that three inhibitors were biosafe and non-cytotoxic against SW1353 cells, precluding their interference with cellular uptake capacity. Subsequently, the ability of cellular C6@Exos uptake after inhibitors intervention was determined by FCM, and the results are shown in Fig. 2D. The presence of GST resulted in a decreased cellular uptake of C6@Exos, compared with the control, CPZ and AMI group. In the statistical MFI plot (Fig. 2E), intuitively, SW1353 cells intervened with GST represented a significant decrease in fluorescence intensity, while that of AMI and CPZ groups were not obviously down. These results suggest that the GST-inhibited endocytic pathway is the main way Exos were uptake by SW1353, that is the caveolin-mediated endocytosis pathway.

### 3.3. Cytoprotective effects of ICA@Exos

In the OA, cell proliferation and migration abilities are decreased, accompanied by an increase in MMP13 secretion, but these changes aggravate cartilage damage. Effective cytoprotection and reduction of associated secretion are the core goals of OA therapy. Therefore, we first investigated the proliferation-promoting effects of the relevant agents. According to the MTT results (Fig. 3A), different concentrations of ICA showed different effects on cell proliferation. After IL-1 $\beta$  treatment, the growth state of inflammatory cells was significantly reduced. However, the apoptosis of SW1353 cells was inhibited, once intervened with low concentration of ICA. With the increase of ICA concentration in a certain range, the cell proliferation rate gradually improved, verifying that appropriate concentration of ICA can accelerate cell proliferation. When the concentration reached 10<sup>-4</sup> M, the cell growth was reversed, so 10<sup>-5</sup> M was selected as the optimal concentration of ICA. Subsequently, the proliferative effects of ICA, BMSC-Exos and ICA@Exos were further investigated at fixed ICA concentrations, and the results are shown in Fig. 3B. SW1353 cells proliferated significantly after ICA and BMSC-Exos intervention alone, clarifying that both of them possess the ability to promote cell proliferation. In addition, ICA@Exos group represented a higher cell proliferation rate compared to the single effect, which was attributed to the cellular delivery capacity of Exos, allowing more efficient cellular uptake and thus a better proliferative effect, and also attributed to the synergistic effect of both within target cells.

The migration ability of SW1353 in response to different agents was further evaluated, and the results were shown in Fig. 3C. As hypothesized, IL-1 $\beta$ , as an inducer of osteoarticular

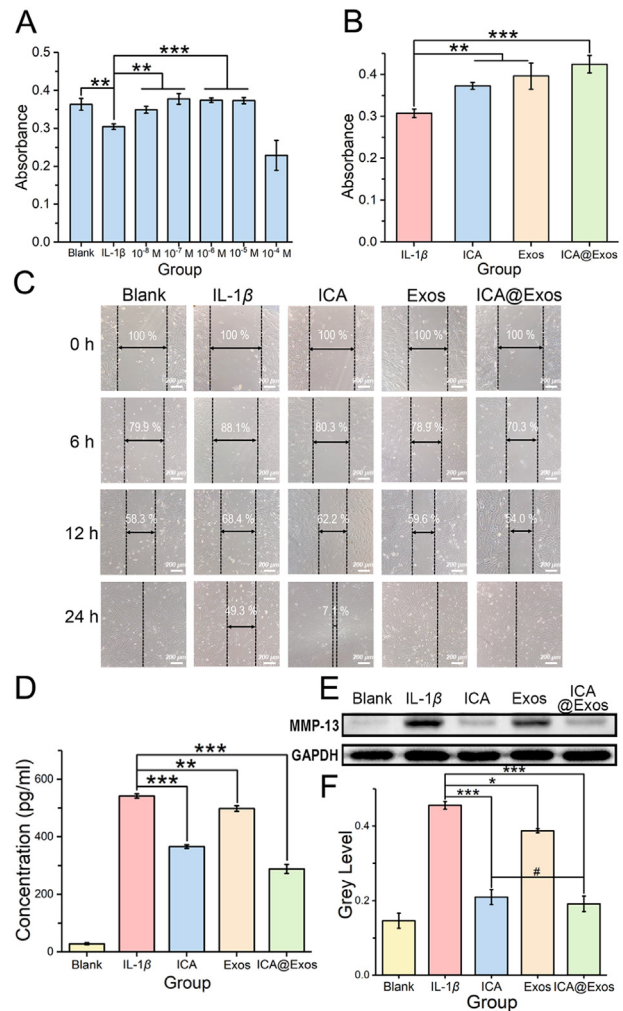


**Fig. 3 – Cytoprotective effects of ICA@Exos for cartilage repair. (A) The proliferation promoting effects of ICA with different concentrations. (B) The proliferation promoting effects of ICA, BMSC-Exos and ICA@Exos. (C) The migration promoting effects of ICA, BMSC-Exos and ICA@Exos. (D) The detection of MMP13 content in the inflammation-induced SW1353 cell supernatant treated with ICA, BMSC-Exos and ICA@Exos by ELISA kits. (E) The detection of MMP13 content in the inflammation-induced SW1353 cells treated with ICA, BMSC-Exos and ICA@Exos by WB. (F) The statistical graphs of WB results by Image J. Statistical significance: \* $P < 0.05$ , \*\* $P < 0.01$ , \*\*\* $P < 0.001$  and # $P < 0.05$ .**

inflammation, significantly reduced the cell migration, with a rate of only 50% at 24 h. And the cell migration rate increased after ICA, BMSC-Exos and ICA@Exos intervention, respectively. At 12 h, the migration rates of ICA and BMSC-Exos groups were 1.27 and 1.20 times that of IL-1 $\beta$  group, which confirmed that ICA and BMSC-Exos separately played a promoting role in the migration of SW1353 cells. Additionally, the migration effect of ICA@Exos was more significant, with rate reaching 54%. Thanks to the promoting effect of ICA and BMSC-Exos on the cell migration and the delivery effect of BMSC-Exos on ICA, ICA@Exos further played the cooperating effect of ICA and BMSC-Exos.

Furthermore, the MMP13 secretion inhibition ability of each agent was investigated by ELISA and WB. In the detection of cell supernatant by ELISA kit, the MMP13 content of each group was determined, and the results are shown in Fig. 3D. Induction of SW1353 cells with IL-1 $\beta$  significantly increased the secretion of MMP13, which is a prominent feature of OA cells. After ICA and BMSC-Exos were intervened alone, the content of MMP13 in cell supernatants was obviously decreased, indicating that both of the agents play a positive role in inhibiting MMP13 secretion. Moreover, the excellent inhibitory effect of ICA highlights its important significance in the field of cartilage repair. While compared with ICA and BMSC-Exos alone, ICA@Exos further reduce the secretion of MMP13, which was only 53% of that induced by IL-1 $\beta$ . Comprehensively, ICA@Exos represented superior potential in inhibiting MMP13 secretion due to synergistic effect. The experimental results of WB are consistent with the above conclusion (Fig. 3E), and the gray level was further measure by Image J software by calculating the gray ratio with corresponding internal reference protein GAPDH to obtain the bar statistical (Fig. 3F). In the three agent groups, the intercellular MMP13 content was all decreased, and especially the expression of MMP13 in ICA@Exos group was only 41% of that IL-1 $\beta$  group, which was close to the blank group. Obviously, ICA@Exos down-regulated the expression of MMP13 and alleviated its secretion, mitigating the occurrence of inflammation.

In summary, ICA and BMSC-Exos exhibited excellent effect of facilitating cartilage repair and regeneration, respectively, and BMSC-Exos, as superior drug delivery carriers with high stability and cell affinity, further improved cellular uptake behavior of ICA. Thus, ICA@Exos could efficiently enter cells and play synergism between the two, showing an integrative effect of promoting cell proliferation and migration and inhibiting MMP13 secretion.

### 3.4. Preparations and characterization of multifunctional hydrogel

The synthesized CAT-C and DF-PEG were validated by FTIR (Fig. S4), UV (Fig. S5) and H-NMR (Fig. S6). In the infrared spectra of CAT-C, a new absorption peak of benzene ring skeleton appeared at 1550 cm<sup>-1</sup>, and absorption peak attributed to =CH appeared at 2980 cm<sup>-1</sup>. As for infrared spectra of DF-PEG, the peaks at 1550, 1697 and 1720 cm<sup>-1</sup> corresponded to benzene ring, -CHO and -COO-. The UV spectrum showed that the characteristic absorption peak of benzene ring appeared in the range of 200–300 cm<sup>-1</sup> for both CAT-C and DF-PEG. Additionally, the HNMR results for CAT-C confirmed the apparent presence of three catechol protons clearly in the 6.62–6.75 ppm range, and the HNMR results for DF-PEG were consistent with our previously published studies. All the above results proved that target groups were successfully grafted onto the polymer chains.

The morphologies of obtained hydrogel were observed by SEM, where the reticular lamellar structure could be clearly seen, verifying its internal structural characteristics (Fig. 4A). Therefore, a schematic diagram of the hydrogel structure was drawn accordingly, as shown in Fig. 4B. The hydrogel framework mainly relies on the interweaving of CS chains and

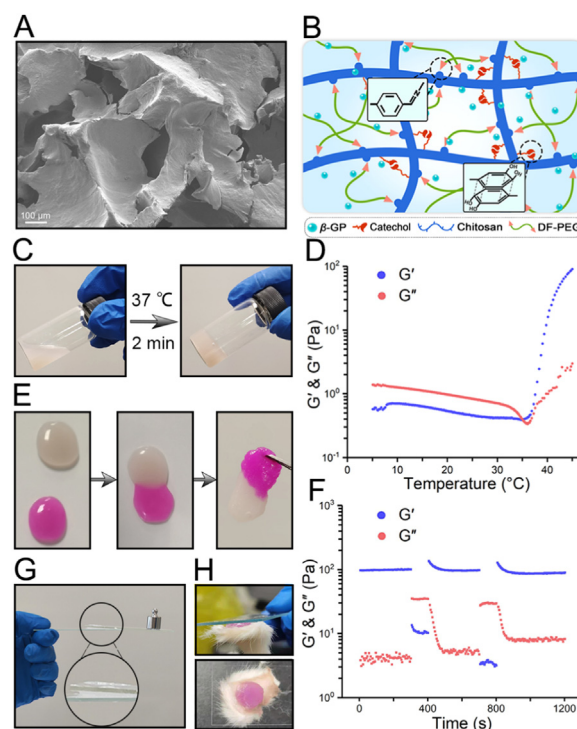


**Fig. 4 – Morphology and structural scheme and multi-properties characterization of “mussel-inspired” multifunctional hydrogel system. (A) The SEM images of internal structure of hydrogels. (B) The structural schematic diagram of hydrogels. (C-D) The macroscopical evaluation and rheological investigation of temperature sensitivity. (E-F) The macroscopical evaluation and rheological investigation of self-healing property. (G) The adhesive property of hydrogels between two layers of slides. (H) The adhesive property of hydrogels between glass and skin tissue.**

the spontaneous formation of various type of bonds, such as imine bonds,  $\pi$ - $\pi$  stacking and hydrogen bonds.

To test the thermosensitivity of hydrogels macroscopically, we first investigated the gelation behavior by inversion method (Fig. 4C). The precursor solution was gelatinized in about 2 min at 37 °C, demonstrating its admirable gelatinizing property. Once the preset temperature is reached, the gelation transformation will occur rapid, and meet the requirements of intra-articular drug delivery. Moreover, the changes of  $G'$  and  $G''$  during the gelation transition were further measured, and the  $T_{sol-gel}$  was determined by the intersection of two curves. As shown in Fig. 4D, where both  $G'$  and  $G''$  increased as temperature rise, with a significant greater rate of  $G'$  than  $G''$ . In the initial stage, the system displayed low elasticity and low viscosity of the solution, where  $G' < G''$ . Later,  $G' = G''$ , and sample was gelated with great elasticity, corresponding to a temperature of 34.7 °C for  $T_{sol-gel}$ . During the gelation, the interaction between CS and  $\beta$ -GP play the dominant role. At low temperatures, electrostatic interactions between the positively charged ammonium groups of CS ( $-NH_3^+$ ) and the phosphate moieties of  $\beta$ -GP ( $-PO_4^-$ ) reduce the electrostatic repulsion and stabilize the solution system. After heating, the

amount of electrostatic charge in CS chains decreases and the hydrophobic interaction is enhanced, which eventually leads to the sol-gel transition [52,61].

For macroscopic self-healing test, two pieces of hydrogels with different colors were placed in contact. After 5 min, the boundary between gels was obviously blurred, with colors fusing, and two gels were rejoined into one whole, which could be lifted by a tweezer. As shown in Fig. 4E, this phenomenon revealed that the hydrogels were able to crosslink spontaneously and maintain the structural integrity with good mechanical property. Subsequently, the rheological data again verified the self-healing property, and the results are shown in Fig. 4F. In dynamic strain step test, the modulus values of hydrogel changed regularly. At low strain,  $G' > G''$ , and samples kept a stable gel state, while at high strain,  $G' < G''$ , indicating the structural damage and morphological changes of hydrogels. The strain mutation caused a mutation in the modulus, but this process didn't affect the performance of hydrogel, that is, hydrogels could quickly recover to the its original state after removal of high strain. As shown in Fig. S7, the excellent self-healing property is attributed to: (1) dynamic imine bonds formed between  $-NH_2$  and  $-CHO$  groups, (2)  $\pi-\pi$  stacking and hydrogen bonding between catechol groups. The multiple dynamic bonds permit the excellent self-healing property, so that the destroyed hydrogels can rapidly crosslink. Additionally, these interactions further enhance the crosslinking degree of hydrogel network and improve the mechanical strength of CS gels. Self-healing property efficiently addresses the challenge of structural damage caused by external forces, extending the duration of hydrogels and making them suitable for administration in the articular cavity.

Furthermore, the adhesiveness of hydrogel was verified. As shown in Fig. 4G, hydrogel produced a strong adhesion force between the two slides to resist a certain weight, without destroying its morphology. Meanwhile, hydrogels isolated from *in vivo* also exhibited excellent adhesion, which could form an adhesive interaction between the skin and the slide (Fig. 4H). This phenomenon proved that the gel injected into the body retained the ideal adhesion after separation from the moist body fluid environment. Even though the adhesive mechanism has not been fully understood, it is certain that the strong wet adhesion depends on both the covalent and non-covalent interactions between catechol groups and various groups on material surfaces. During joint inflammation, synovial fluid increases, making it difficult for the conventional hydrogels to form tight adhesion with tissues under wet conditions. Therefore, adhesive hydrogels address this problem and enhance effective adhesion and retention at the joint cavity. The strong tissue adhesion avoids hydrogels detachment from the surrounding cartilage tissue after implantation, thereby promoting the integration of hydrogels with the defective cartilage tissue and the formation of new tissue.

### 3.5. *In vitro* degradation and *in vivo* gelation behavior of hydrogel, and *in vitro* safety evaluation of hydrogel

In the complicated inflammatory environment, various enzymes and factors will accelerate the erosion of hydrogel

structure, leading to the rapid release of the contents in the hydrogels. Hence, it is indispensable to endow hydrogel with the capability of resistance to erosion and protection of structural integrity. As shown in Fig. 5A, the residual amount of CCGD hydrogels still maintained at about 63% on Day 21, with a significant lower degradation rate than CCG hydrogels. Additionally, the *in vivo* degradation behavior was studied in Fig. S8. After 7 d of subcutaneous injection on the back of rats, CCGD and CGD gels remained in good gel states, but there was some shrinkage in volume, which was due to the gel water loss and degradation caused by internal metabolism and fluid reequilibration. In contrast, the degradation of CCG gels was significant, of which the low crosslinking degree leads to the poor mechanical strength and rapid degradation rate. There are complex chemical and physical crosslinks in CCGD hydrogels, including imine bonds,  $\pi-\pi$  stacking and hydrogen bonds, which could effectively promote the hydrogel systems to resist degradation and remain stable in target site for a long time.

In addition, the *in vivo* gelation process of hydrogels was further observed by subcutaneous injection. During the injection, the CCGD hydrogel precursor solution could enter the subcutaneous tissue smoothly without obvious resistance, and quickly form spherical protrusions, proving its excellent injectability and fluidity. After 5 min, the formation of hydrogel clumps could be seen in the isolated skin, as shown in Fig. 5B. Subsequently, the three hydrogels were stripped. Compared with CCG hydrogels, CCGD and CGD hydrogels were tighter with clearer boundaries, and the hydrogel masses had higher mechanical strength (Fig. 5C). Moreover, CCGD hydrogels also exhibited superior adhesion properties. All these results suggested that CCGD hydrogel systems rapidly gelate once injected into the articular cavity, facilitating the formation of a suitable *in situ* drug reservoir.

Next, the cytotoxicity of the serial blank hydrogel extractive solutions were measured by MTT assay, and the results of cell viability were displayed in Fig. 5D. The cell survival rate of each concentration group was more than 90%, indicating the admirable biocompatibility and non-cytotoxicity of the hydrogel. The hemolytic activity of blank hydrogels was then tested, and the results of the three different concentrations extractive solutions was shown in Fig. 5E and 5F. The hemolysis rate of each group was lower than 5%, and almost no hemolysis phenomenon was observed, which again proved the superior biological safety of hydrogels. Summarily, the hydrogel system is an ideal carrier material that is mild to the defective cartilage tissue and produce none additional inflammatory responses.

Subsequently, the hydrogels were subjected to 3D culture of SW1353 cells for 12 h, 24 h and 72 h, and the cell distribution inside hydrogels was shown in Fig. 5G. Live cells were stained with Calcein dye, and labeled to give them a green color. At 12 h, cells were successfully transferred from the liquid culture medium to the surface layer of hydrogels, thus obvious fluorescence distribution was observed on the hydrogel surfaces. The above phenomena are attributed to the abundance of catechol groups, which endows hydrogels with excellent cell affinity and the ability

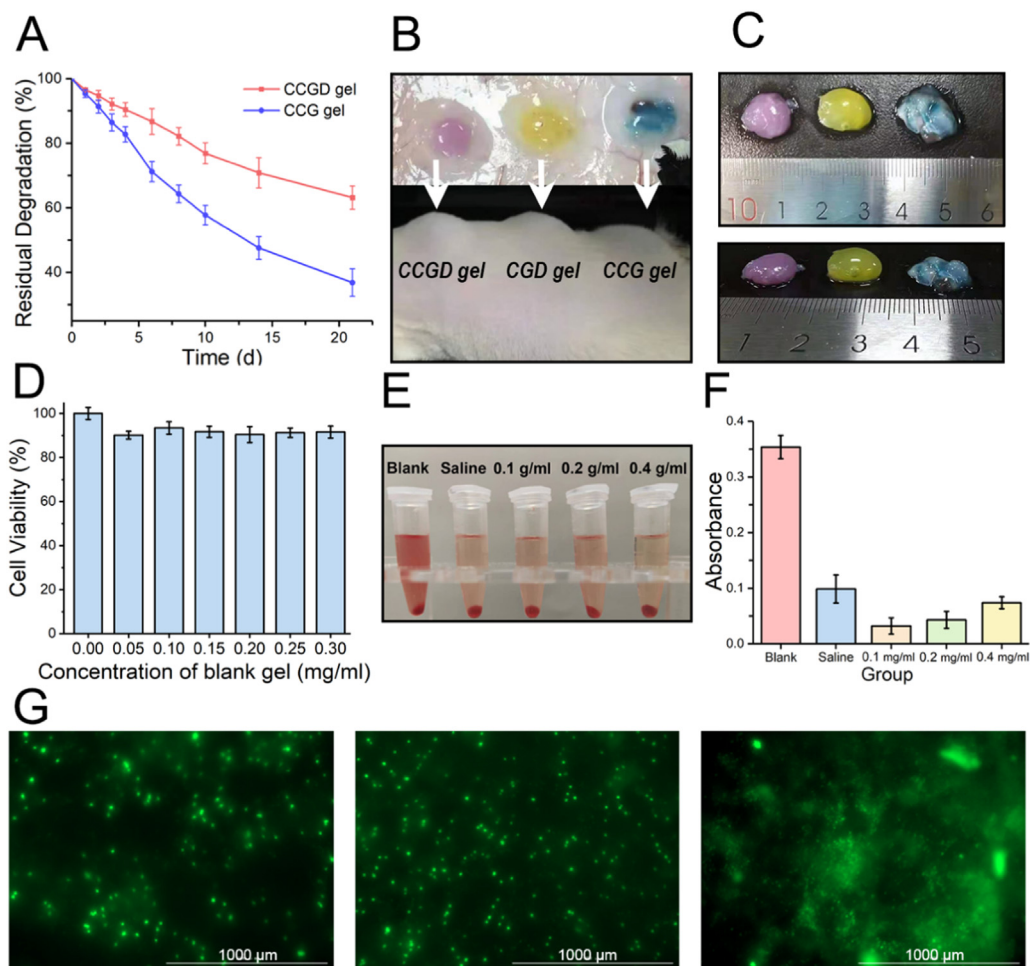


**Fig. 5 – The degradation and gelation behavior investigation of hydrogels, in vitro safety and cell culture evaluation of hydrogels. (A) The in vitro degradation curve of hydrogels. (B-C) The in vivo gelation results of hydrogels. (D) The cytotoxicity of blank hydrogel extractive solutions with different concentrations. (E-F) The hemolytic test results of hydrogels. (G) The 3D cell culture results and cell distribution within hydrogels observed by staining with Calcein dye (green refers to live cells).**

to recruit cells from surrounding environment. When the incubation time was extended to 24 h, the fluorescence density on the surface layer of hydrogels significantly increased, indicating that the cells maintained a good growth and proliferation state in the hydrogels. After 72 h of culture, the green fluorescence was further dense and deeper into the hydrogels, showing a higher cell density and an increased cell growth depth inside hydrogels. Therefore, combining with superior biocompatibility and adhesion, hydrogels provide an admirable environment for cells, and can even serve as a cellular matrix [56,62]. The proper adhesion allows hydrogels to effectively attract and host the surrounding cells, while the appropriate pore size guarantees the cell migration inside the hydrogels. The high protein affinity of catechol group resulted in more efficient and stable immobilization of the signal proteins to establish a positive feedback loop on the signaling cascade, promoting the growth of new cartilage tissue. Additionally, the tight binding between hydrogels and tissues further facilitates the migration of cells to the tissue defects, and promotes the regeneration of the target tissue.

### 3.6. In vitro encapsulation and release, and in vivo safety assessment of ICA@Exos-loaded hydrogel

The encapsulation capacity and release behavior of ICA@Exos-loaded hydrogels were evaluated. The 3D distribution of Dio-labeled ICA@Exos within the hydrogels was observed by CLSM, and the results are shown in Fig. 6A. ICA@Exos were uniformly distributed within the hydrogels without agglomeration, and almost no sedimentation was seen during the observation period, indicating that an evenly distributed ICA@Exos-loaded hydrogel was successfully prepared.

In addition, the release kinetics of ICA-loaded and ICA@Exos-loaded hydrogels were measured respectively, and the results are shown in Fig. 6B. In the release curve of ICA-loaded hydrogels, ICA release reached saturation on Day 4, and the cumulative release was less than 50%. Due to the low water solubility, ICA will aggregate in the aqueous environment inside hydrogels, and cannot be completely released, with a large proportion of ICA still retaining in the hydrogels. Therefore, for the delivery of insoluble drugs,

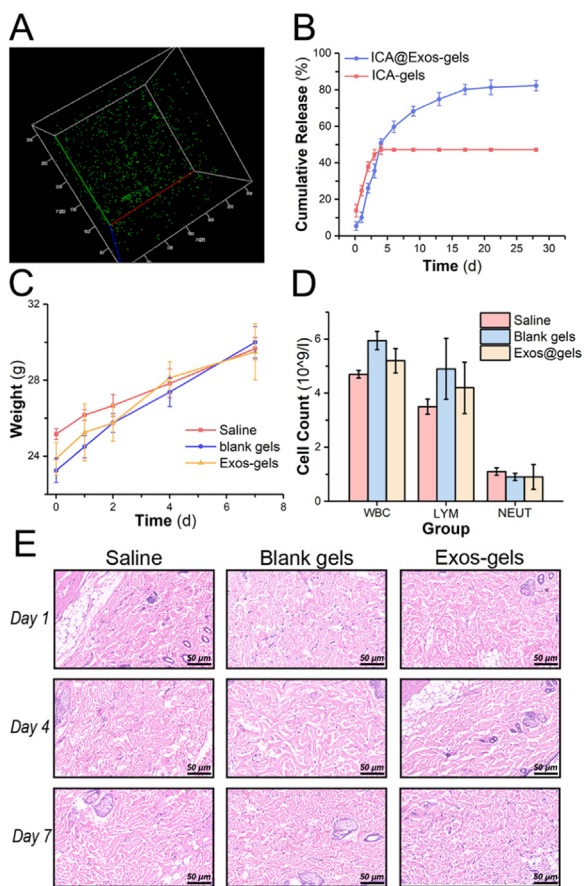


**Fig. 6 – The encapsulation capacity and release behavior evaluation, and in vivo biosafety assessment of ICA@Exos-loaded hydrogels. (A) The images of ICA@Exos distribution within hydrogels by CLSM (green refers to ICA@Exos). (B) The release kinetics of ICA-loaded and ICA@Exos-loaded hydrogels. (C) The plot of weight changes in ICR mice treated with saline, blank gels and Exos-gels. (D) The results of blood routine test of ICR mice treated with saline, blank gels and Exos-gels. (E) The histological H&E staining images of the subcutaneous tissue surrounding the hydrogels at different time points treated with saline, blank gels and Exos-gels.**

simple hydrogel encapsulation fails to achieve the purpose of sustained release of drugs and hinders the efficacy of drugs. As for the ICA@Exos-loaded hydrogels, the drug release rate was stable, and the cumulative release reached 82% with 28 d of continuous release behavior. This phenomenon demonstrates that ICA was stably encapsulated in Exos and released sustainably, rather than leaking and aggregating in the gel matrix. In addition, the drug release was dominated by diffusion, and the reticular structure of hydrogel closely affected the release rate of Exos. The release behavior lasted for 4 weeks, indicating that the mesh size of the gel is favorable for the effective retention and excellent release of ICA@Exos inside the gel. Hence, ICA@Exos-loaded hydrogels is able to form a potential drug reservoir at joint cavity for sustained release, so as to play a long-term effect on OA treatment.

The *in vivo* biological safety was further assessed by different models and experiments. Taking ICA mice as subjects, the changes in body weight after subcutaneous injection were monitored, and the results are shown in Fig. 6C. There was no significant difference in the data among the saline group, blank hydrogel group and ICA@Exos-loaded hydrogel group, and the body weight of mice in all the three groups increased steadily. Additionally, the number of white blood cell (WBC), lymphocyte (LYM) and neutrophil (NEUT) were selected as the judgment indicators of inflammation in mice detected by blood routine, and the results are shown in Fig. 6D. In each group, the counts of the three types of inflammation-related cells were within the normal range, and the differences were not statistically significant, indicating that no inflammatory response occurred. The biosafety of the ICA@Exos-loaded hydrogel was preliminarily verified by *in vivo* evaluation in mice.

Furthermore, the *in vivo* safety of blank hydrogel and ICA@Exos-loaded hydrogel in SD rats was observed by H&E staining. The skin tissue at the injection site was studied histologically after 1, 4 and 7 d, and the results are shown in Fig. 6E. There was no obvious inflammatory cell infiltration in the skin sections obtained at different time points in the three groups, confirming the high biocompatibility and low cytotoxicity of this system. All the *in vivo* safety studies proved that ICA@Exos-loaded hydrogels is a potential and safe drug delivery carrier.

### 3.7. *In vivo* retention and OA improvement ability by ICA@Exos-loaded hydrogel

The retention behavior of Exos without scaffold and Exos embedded into hydrogels was separately evaluated, and the Exos were tracked by DiR fluorescence signal. As the results shown in Fig. 7A, it was obvious that the fluorescence attenuation rate of the hydrogel delivery group was relatively slower, and the statistical plot of fluorescence intensity was presented in Fig. S9. In the ICA@Exos direct administration group, the fluorescence intensity decreased significantly on Day 4 and was extremely low on Day 7. By comparing the fluorescence intensity changes of the two groups, it could be intuitively found that the Exos incorporated into hydrogels avoided rapid clearance, and the hydrogels, serving as an admirable scaffold, are able to significantly prolong the retention and enhance the stability of Exos *in vivo*, thus exerting the long-term effects of ICA@Exos. As reported in literature, the rapid clearance and low stability of Exos limit their further utilization, but hydrogels present a potential carrier to enhance Exos retention. In particular, multi-functional hydrogels better match the physiological properties of the target tissue, and successfully maintain their long-term stability in the inflamed joint environment.

After the OA rat models were successfully constructed, the interventions were administrated in the four groups, respectively. Five weeks later, all the SD rats were sacrificed, and the joint samples were collected for SO-FG, TB and H&E staining, and the representative images of each group were displayed in Fig. 7B. The samples in saline group exhibited obvious signs of cartilage degeneration, which was the typical and clear manifestation of OA, including matrix

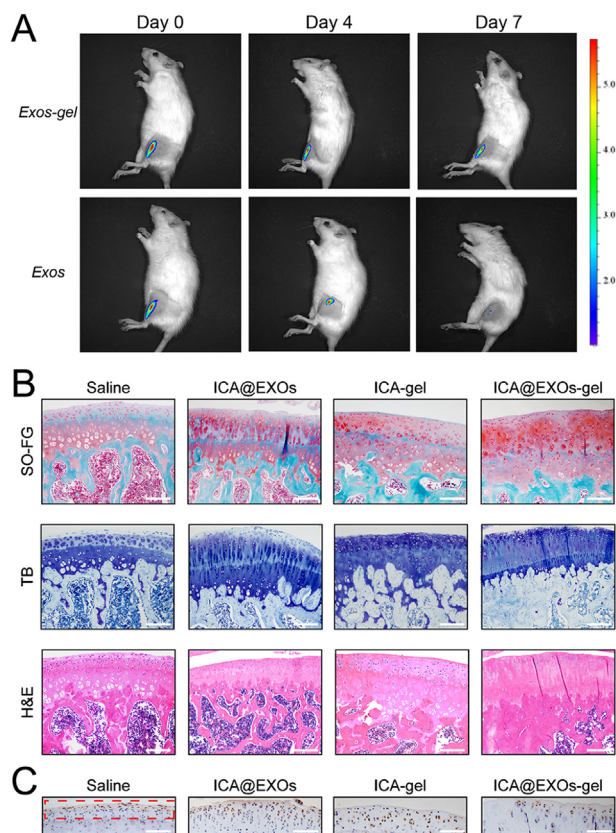


**Fig. 7 – The retention ability evaluation, and in vivo pharmacodynamic studies of ICA@Exos-loaded hydrogels. (A) The retention behavior of Exos embedded into hydrogels. (B) SO-FG, TB and H&E staining images of joint samples with different treatment in histological analysis. (C) The immunohistochemical staining images for MMP13 of joint samples with different treatment (scale bar =100  $\mu$ m).**

degradation and abrasion. In contrast, the thickness and density of the cartilage matrix in ICA@Exos group and ICA-gel group increased, confirming that both of them could effectively slow down the degenerative process of cartilage. Moreover, the cartilage repair effects of ICA-gel were more significant, which was related to the shorter retention time of Exos and the long-term storage effect of hydrogels at the target site. Similarly, after ICA@Exos-gel treatment, cartilage tissue staining was more pronounced, and obvious cartilage regeneration and surface smooth could be observed clearly. The pharmacodynamic study *in vivo* verified the excellent chondroprotective effect of ICA@Exos-loaded hydrogel, that the ICA and Exos could exert a synergistic effect on the cartilage repair, while the hydrogel could ensure the stable existence of the system and sustained drug release in the joint cavity. Furthermore, the downregulation degree of MMP13 was evaluated by IHC as shown in Fig. 7C. The expression of MMP13 in each group could be clearly observed in the cartilage region of each section. The rate of MMP13-positive cells in the saline group was the highest, approaching 50%, while the ICA@Exos-gel group had the lowest MMP13 expression.

Likewise, the MMP13 contents of cartilage region in ICA@Exos and ICA-gel groups were between the middle value, consistent with the previous experimental results. Taken together, all these results revealed the positive effects of ICA@Exos-loaded hydrogels on cartilage protection *in vivo*, alleviating the cartilage degeneration and accelerating the cartilage repair.

#### 4. Conclusion

Persistent articular cartilage damage is the hallmark of OA, and promoting cartilage regeneration is one of the key links to solve OA. As a component of traditional Chinese medicine (TCM), ICA has multi-target and multi-channel pharmacological effects on cartilage repair with few adverse reactions. However, similar to most TCM components, their low bioavailability limits their efficacy. BMSC-Exos are rich in active ingredients and possess a high potential as cell-free factors for OA treatment. Likewise, Exos act as mediums of cell communication, which are able to achieve drug delivery into cells. Herein, BMSC-Exos were used as cellular delivery carrier of ICA to improve the cellular uptake efficiency of ICA and further play synergistic effect on cartilage repair, including promoting cell proliferation and migration and inhibiting MMP13 secretion. The major challenge of this primary system is to achieve long-term retention in the joint cavity, especially in the inflammatory environment. As an important intra-articular drug delivery system, hydrogels can be used for long-term analgesia and anti-inflammation. On the basis of syringeability, the hydrogels are further endowed with self-healing and adhesion properties. In the highly active joint regions, the ability to rapidly and spontaneously cross-link allows hydrogels to maintain structural stability and integrity. The “mussel-inspired” adhesiveness makes hydrogels adhere better to the wet cartilage surface and facilitates the cell attachment and migration, thus promoting the cartilage regeneration. The resulting ICA@Exos-loaded hydrogel system efficiently combines the three parts, eliminates the shortcomings of a single part, and enables each part to act synergistically to play a significant role in cartilage repair.

#### Conflicts of interest

The authors report no conflicts of interest. The authors are responsible for the content and writing of this paper.

#### Supplementary materials

Supplementary material associated with this article can be found, in the online version, at [doi:10.1016/j.ajps.2023.100799](https://doi.org/10.1016/j.ajps.2023.100799).

#### REFERENCES

- [1] Glyn-Jones S, Palmer AJR, Agricola R, Price AJ, Vincent TL, Weinans H, et al. Osteoarthritis. *Lancet* 2015;386(9991):376–87.

- [2] Sharma L. Osteoarthritis of the knee. *New Engl J Med* 2021;384:51–9.
- [3] Guilak F, Nims RJ, Dicks A, Wu CL, Meulenbelt I. Osteoarthritis as a disease of the cartilage pericellular matrix. *Matrix Biol* 2018;71-72:40–50.
- [4] Peng Z, Sun H, Bunpetch V, Koh YW, Wen Y, Wu DM, et al. The regulation of cartilage extracellular matrix homeostasis in joint cartilage degeneration and regeneration. *Biomaterials* 2021;268:120555.
- [5] Shi YY, Hu XQ, Cheng J, Zhang X, Zhao FY, Shi WL, et al. A small molecule promotes cartilage extracellular matrix generation and inhibits osteoarthritis development. *Nat Commun* 2019;10:1914.
- [6] Mehana ESE, Khafaga AF, El-Blehi SS. The role of matrix metalloproteinases in osteoarthritis pathogenesis: an updated review. *Life Sci* 2019;234:116786.
- [7] Zhang H, Cai D, Bai X. Macrophages regulate the progression of osteoarthritis. *Osteoarthr Cartilage* 2020;28:555–61.
- [8] Hu QC, Ecker M. Overview of MMP-13 as a promising target for the treatment of osteoarthritis. *Int J Mol Sci* 2021;22(4):1742.
- [9] Mobasheri A, Rayman MP, Gualillo O, Sellam J, van der Kraan P, Fearon U. The role of metabolism in the pathogenesis of osteoarthritis. *Nat Rev Rheumatol* 2017;13(5):302–11.
- [10] Wei W, Ma YZ, Yao XD, Zhou WY, Wang XZ, Li CL, et al. Advanced hydrogels for the repair of cartilage defects and regeneration. *Bioact Mater* 2021;6(4):998–1011.
- [11] Li CR, Li Q, Mei QB, Lu TL. Pharmacological effects and pharmacokinetic properties of icariin, the major bioactive component in *Herba Epimedii*. *Life Sci* 2015;126:57–68.
- [12] Feng Q, Xu JK, Zhang KY, Yao H, Zheng NY, Zheng LZ, et al. Dynamic and cell-infiltratable hydrogels as injectable carrier of therapeutic cells and drugs for treating challenging bone defects. *Acs Central Sci* 2019;5(3):440–50.
- [13] Zhou LP, Poon CCW, Wong KY, Cao SS, Dong XL, Zhang Y, et al. Icarin ameliorates estrogen-deficiency induced bone loss by enhancing IGF-I signaling via its crosstalk with non-genomic ER $\alpha$  signaling. *Phytomedicine* 2021;82:153413.
- [14] Wang Z, Wang D, Yang D, Zhen W, Zhang J, Peng S. The effect of icariin on bone metabolism and its potential clinical application. *Osteoporosis Int* 2018;29(3):535–44.
- [15] Zeng NX, Li HZ, Wang HZ, Liu KG, Gong XY, Luo WL, et al. Exploration of the mechanism by which icariin modulates hippocampal neurogenesis in a rat model of depression. *Neural Regen Res* 2022;17(3):632–42.
- [16] Jin J, Wang H, Hua XY, Chen DJ, Huang C, Chen Z. An outline for the pharmacological effect of icariin in the nervous system. *Eur J Pharmacol* 2019;842:20–32.
- [17] Tan HL, Chan KG, Pusparajah P, Saokaew S, Duangjai A, Lee LH, et al. Anti-cancer properties of the naturally occurring aphrodisiacs: icariin and its derivatives. *Front Pharmacol* 2016;7:191.
- [18] Zhang JT, Fan FY, Liu AF, Zhang C, Li Q, Zhang CL, et al. Icarin: a potential molecule for treatment of knee osteoarthritis. *Front Pharmacol* 2022;13:811808.
- [19] Zhang JT, Zhang DL, Wu CC, Liu AF, Zhang C, Jiao JJ, et al. Icarin-conditioned serum engineered with hyaluronic acid promote repair of articular cartilage defects in rabbit knees. *Bmc Complem Altern M* 2019;19:155.
- [20] Liu YB, Yang JR, Luo ZC, Li DX, Lu J, Wang QG, et al. Development of an injectable thiolated icariin functionalized collagen/hyaluronic hydrogel to promote cartilage formation *in vitro* and *in vivo*. *J Mater Chem B* 2019;7(17):2845–54.
- [21] Liu N, Zhang T, Cao BR, Luan FY, Liu RX, Yin HR, et al. Icarin possesses chondroprotective efficacy in a rat model of dexamethasone-induced cartilage injury through the activation of miR-206 targeting of cathepsin K. *Int J Mol Med* 2018;41(2):1039–47.
- [22] Zhao CF, Li ZH, Li SJ, Li JA, Hou TT, Wang Y. PLGA scaffold carrying icariin to inhibit the progression of osteoarthritis in rabbits. *Roy Soc Open Sci* 2019;6(4):181877.
- [23] Mancuso P, Raman S, Glynn A, Barry F, Murphy JM. Mesenchymal stem cell therapy for osteoarthritis: the critical role of the cell secretome. *Front Bioeng Biotech* 2019;7:9.
- [24] Armiento AR, Alini M, Stoddart MJ. Articular fibrocartilage - why does hyaline cartilage fail to repair? *Adv Drug Deliver Rev* 2019;146:289–305.
- [25] Zhang B, Yin YJ, Lai RC, Tan SS, Choo ABH, Lim SK. Mesenchymal stem cells secrete immunologically active exosomes. *Stem Cells Dev* 2014;23(11):1233–44.
- [26] Liang YJ, Duan L, Lu JP, Xia J. Engineering exosomes for targeted drug delivery. *Theranostics* 2021;11(7):3183–95.
- [27] Yang BW, Chen Y, Shi JL. Exosome biochemistry and advanced nanotechnology for next-generation theranostic platforms. *Adv Mater* 2019;31(2):1802896.
- [28] Zhang Y, Liu YF, Liu HY, Tang WH. Exosomes: biogenesis, biologic function and clinical potential. *Cell Biosci* 2019;9:19.
- [29] Guan PF, Liu C, Xie DH, Mao SC, Ji YL, Lin YC, et al. Exosome-loaded extracellular matrix-mimic hydrogel with anti-inflammatory property facilitates/promotes growth plate injury repair. *Bioact Mater* 2022;10:145–58.
- [30] Zhou QF, Cai YZ, Jiang YZ, Lin XJ. Exosomes in osteoarthritis and cartilage injury: advanced development and potential therapeutic strategies. *Int J Biol Sci* 2020;16(11):1811–20.
- [31] Bao CC, He CQ. The role and therapeutic potential of MSC-derived exosomes in osteoarthritis. *Arch Biochem Biophys* 2021;710:109002.
- [32] Acharya C, Adesida A, Zajac P, Mumme M, Riesle J, Martin I, et al. Enhanced chondrocyte proliferation and mesenchymal stromal cells chondrogenesis in coculture pellets mediate improved cartilage formation. *J Cell Physiol* 2012;227(1):88–97.
- [33] Antimisiaris SG, Mourtas S, Marazioti A. Exosomes and exosome-inspired vesicles for targeted drug delivery. *Pharmaceutics* 2018;10(4):218.
- [34] Akuma P, Okagu OD, Udenigwe CC. Naturally occurring exosome vesicles as potential delivery vehicle for bioactive compounds. *Front Sustain Food S* 2019;3:23.
- [35] Li SP, Lin ZX, Jiang XY, Yu XY. Exosomal cargo-loading and synthetic exosome-mimics as potential therapeutic tools. *Acta Pharmacol Sin* 2018;39(4):542–51.
- [36] Cheng JY, Chen Z, Liu C, Zhong M, Wang SH, Sun YJ, et al. Bone mesenchymal stem cell-derived exosomes-loaded injectable hydrogel for minimally invasive treatment of spinal cord injury. *Nanomedicine* 2021;16(18):1567–79.
- [37] Monguio-Tortajada M, Prat-Vidal C, Moron-Font M, Clos-Sansalvador M, Calle A, Gastelurrutia P, et al. Local administration of porcine immunomodulatory, chemotactic and angiogenic extracellular vesicles using engineered cardiac scaffolds for myocardial infarction. *Bioact Mater* 2021;6(10):3314–27.
- [38] Zhou YJ, Liu SY, Zhao M, Wang CS, Li L, Yuan YJ, et al. Injectable extracellular vesicle-released self-assembling peptide nanofiber hydrogel as an enhanced cell-free therapy for tissue regeneration. *J Control Release* 2019;316:93–104.
- [39] Yang YL, Zhu ZC, Gao RZ, Yuan J, Zhang JT, Li HY, et al. Controlled release of MSC-derived small extracellular vesicles by an injectable Diels-Alder crosslinked hyaluronic acid/PEG hydrogel for osteoarthritis improvement. *Acta Biomater* 2021;128:163–74.
- [40] Fan L, Liu C, Chen XX, Zheng L, Zou Y, Wen HQ, et al. Exosomes-loaded electroconductive hydrogel synergistically promotes tissue repair after spinal cord injury via immunoregulation and enhancement of myelinated axon growth. *Adv Sci* 2022;9(13):2105586.

- [41] Li QT, Xu S, Feng Q, Dai QY, Yao LT, Zhang YC, et al. 3D printed silk-gelatin hydrogel scaffold with different porous structure and cell seeding strategy for cartilage regeneration. *Bioact Mater* 2021;6(10):3396–410.
- [42] Liu M, Zeng X, Ma C, Yi H, Ali Z, Mou XB, et al. Injectable hydrogels for cartilage and bone tissue engineering. *Bone Res* 2017;5:17014.
- [43] Qiao ZG, Lian MF, Han Y, Sun BB, Zhang X, Jiang WB, et al. Bioinspired stratified electrowritten fiber-reinforced hydrogel constructs with layer-specific induction capacity for functional osteochondral regeneration. *Biomaterials* 2021;266:120385.
- [44] Reakasame S, Boccaccini AR. Oxidized alginate-based hydrogels for tissue engineering applications: a review. *Biomacromolecules* 2018;19(1):3–21.
- [45] Zhang YB, Yu JK, Ren KX, Zuo JL, Ding JX, Chen XS. Thermosensitive hydrogels as scaffolds for cartilage tissue engineering. *Biomacromolecules* 2019;20(4):1478–92.
- [46] Shen YF, Xu GZ, Huang HX, Wang KY, Wang H, Lang MD, et al. Sequential release of small extracellular vesicles from bilayered thiolated alginate/polyethylene glycol diacrylate hydrogels for scarless wound healing. *ACS Nano* 2021;15(4):6352–68.
- [47] Mardpour S, Ghanian MH, Sadeghi-Abandansari H, Mardpour S, Nazari A, Shekari F, et al. Hydrogel-mediated sustained systemic delivery of mesenchymal stem cell-derived extracellular vesicles improves hepatic regeneration in chronic liver failure. *ACS Appl Mater Inter* 2019;11(41):37421–33.
- [48] Mol EA, Lei ZY, Roefs MT, Bakker MH, Goumans MJ, Doevendans PA, et al. Injectable supramolecular ureidopyrimidinone hydrogels provide sustained release of extracellular vesicle therapeutics. *Adv Healthc Mater* 2019;8(20):1900847.
- [49] Chen PF, Zheng L, Wang YY, Tao M, Xie Z, Xia C, et al. Desktop-stereolithography 3D printing of a radially oriented extracellular matrix/mesenchymal stem cell exosome bioink for osteochondral defect regeneration. *Theranostics* 2019;9(9):2439–59.
- [50] Chen JG, Huang TY, Liu RQ, Wang CY, Jiang HY, Sun HY. Congenital microtia patients: the genetically engineered exosomes released from porous gelatin methacryloyl hydrogel for downstream small RNA profiling, functional modulation of microtia chondrocytes and tissue-engineered ear cartilage regeneration. *J Nanobiotechnol* 2022;20(1):164.
- [51] Zhang Y, Wang XW, Chen J, Qian DF, Gao P, Qin T, et al. Exosomes derived from platelet-rich plasma administration in site mediate cartilage protection in subtalar osteoarthritis. *J Nanobiotechnol* 2022;20(1):56.
- [52] Zeng J, Mamitimin M, Song Y, Sun WB, Wu ZH, Qi XL. Chairside administrated antibacterial hydrogels containing berberine as dental temporary stopping for alveolar ridge preservation. *Eur Polym J* 2021;160:110808.
- [53] Seo BB, Kwon Y, Kim J, Hong KH, Kim SE, Song HR, et al. Injectable polymeric nanoparticle hydrogel system for long-term anti-inflammatory effect to treat osteoarthritis. *Bioact Mater* 2022;7:14–25.
- [54] Xue X, Hu Y, Deng YH, Su JC. Recent advances in design of functional biocompatible hydrogels for bone tissue engineering. *Adv Funct Mater* 2021;31(19):2009432.
- [55] Taylor DL, Panhuis MIH. Self-healing hydrogels. *Adv Mater* 2016;28(41):9060–93.
- [56] Han L, Wang MH, Li PF, Gan DL, Yan LW, Xu JL, et al. Mussel-inspired tissue-adhesive hydrogel based on the polydopamine-chondroitin sulfate complex for growth-factor-free cartilage regeneration. *ACS Appl Mater Inter* 2018;10(33):28015–26.
- [57] Xie CM, Wang X, He H, Ding YH, Lu X. Mussel-inspired hydrogels for self-adhesive bioelectronics. *Adv Funct Mater* 2020;30(25):1909954.
- [58] Gan DL, Xu T, Xing WS, Ge X, Fang LM, Wang KF, et al. Mussel-inspired contact-active antibacterial hydrogel with high cell affinity, toughness, and recoverability. *Adv Funct Mater* 2019;29(1):1805964.
- [59] Hosaka Y, Saito T, Sugita S, Hikata T, Kobayashi H, Fukai A, et al. Notch signaling in chondrocytes modulates endochondral ossification and osteoarthritis development. *P Natl Acad Sci USA* 2013;110(5):1875–80.
- [60] Lee YJ, Kim SA, Lee SH. Hyaluronan suppresses lidocaine-induced apoptosis of human chondrocytes *in vitro* by inhibiting the p53-dependent mitochondrial apoptotic pathway. *Acta Pharmacol Sin* 2016;37(5):664–73.
- [61] Zhou HY, Jiang LJ, Cao PP, Li JB, Chen XG. Glycerophosphate-based chitosan thermosensitive hydrogels and their biomedical applications. *Carbohydr Polym* 2015;117:524–36.
- [62] Xiong YS, Zhang XR, Ma XT, Wang WQ, Yan FY, Zhao XH, et al. A review of the properties and applications of bioadhesive hydrogels. *Polym Chem* 2021;12(26):3721–39.